

Photochemistry dominates over photothermal effects in the laser-induced reduction of graphene oxide by visible light

Received: 13 November 2023

Accepted: 15 October 2024

Published online: 09 November 2024

 Check for updates

Maxim Fatkullin¹, Dmitry Cheshev¹, Andrey Averkiev¹, Alina Gorbunova¹, Gennadiy Murastov², Jianxi Liu³, Pavel Postnikov¹, Chong Cheng⁴✉, Raul D. Rodriguez¹✉ & Evgeniya Sheremet¹

Graphene oxide (GO) possesses specific properties that are revolutionizing materials science, with applications extending from flexible electronics to advanced nanotechnology. A key method for harnessing GO's potential is its laser-induced reduction, yet the exact mechanisms – photothermal versus photochemical effects – remain unclear. Herein, we discover the dominant role of photochemical reactions in the laser reduction of GO under visible light, challenging the prevailing assumption that photothermal effects are dominant. Employing a combination of Raman thermometry, X-ray photoelectron and photoluminescence spectroscopies, and electrical atomic force microscopy, we quantify the temperature and map the reduction process across micro and nano scales. Our findings demonstrate that the photochemical cleavage of oxygen-containing groups below a reduction threshold temperature is a decisive factor in GO reduction, leading to distinct characteristics that cannot be replicated by heating alone. This work clarifies the fundamental mechanisms of GO transformation under visible laser irradiation, highlighting the dominant role of photochemical processes. Distinguishing these subtleties enables the development of laser-reduced GO platforms for graphene-based applications compatible with industrial scales. We illustrate this potential by encoding information on GO surfaces as optical storage, allowing us to write binary sequences in long-term memory encoding invisible even through an optical microscope.

The versatility and exceptional properties of GO have made it a transformative material in nanotechnology and materials science, especially given its applications ranging from sensors and energy storage devices to glass electronics^{1,2}. A crucial area of research is the laser reduction of GO, which is one of the most promising approaches to transition reduced graphene oxide (rGO) from lab to industrial applications. Laser chemistry covers a vast array of materials

from inorganic to organic³ and has been critical in advancing our understanding of materials like GO^{4–6}. One of the major challenges is discerning the primary driver of the chemical transformation during laser irradiation, whether it is laser-induced heating, direct photochemistry, or a combination of both^{7,8}. This question is particularly pressing when considering the laser modification of functionalized graphene⁹.

¹Tomsk Polytechnic University, Lenina ave. 30, Tomsk 634050, Russia. ²University of Mining Leoben, Franz Josef-Straße 18, 8700 Leoben, Austria. ³School of Materials Science and Engineering, Northwestern Polytechnical University, Xi'an 710072, China. ⁴College of Polymer Science and Engineering, State Key Laboratory of Polymer Materials Engineering, Sichuan University, Chengdu 610065, China. ✉e-mail: chong.cheng@scu.edu.cn; raul@tpu.ru

The reduction process of GO is generally understood to involve both photothermal and photochemical contributions^{4–6}. The photothermal one originates from the absorption of incident photons, leading to local heating. This heating provides the energy required to remove oxygen-containing groups, mostly considered to start at $\approx 200\text{ }^\circ\text{C}$ ^{7,8}. Conversely, the photochemical mechanism is proposed to involve light providing the activation energy needed to break chemical bonds selectively, where the commonly agreed threshold is 3.2 eV due to the binding energy of epoxy groups^{6,10,11}. Moreover, the nonuniform structure of GO, with functional groups distributed across its basal plane and edges, adds complexity to the reduction process¹². It was shown that this nonuniform functional group distribution results in semiconducting sp^2 clusters surrounded by a dielectric sp^3 matrix. Light irradiation could initiate the photoreduction process by the photogeneration of electrons (π^* conduction band) and holes (π valence band) through a 2.4 eV to ≈ 4 eV (450–310 nm) band gap^{13,14}. Some studies suggest that basal-plane groups are the primary photo-reactive sites during photochemical reduction¹², while others argue for an alternative reduction sequence¹⁵. Furthermore, the reduction process and stability of the GO film could be strongly affected by the substrate used. For instance, using metallic substrates results in the penetration of metal ions into the GO structure, leading to higher stability than GO films on teflon¹⁶. On the other hand, it was reported that the structural properties of GO itself (content of functional groups and its amount) depend on the synthetic route and ripening time, adding more complexity to the mechanistic understanding of the reduction process. Moreover, the commercial GO synthesized following the modified Hummers method could appear in different states with different structural properties¹⁷.

Various studies have presented diverging views on the GO reduction process. For instance, while some research indicates that thermal reduction begins at temperatures as low as 90–150 $^\circ\text{C}$ ^{18,19}, others contend that only water desorption happens within this temperature range^{20,21}. The role of photon energy, especially in photochemical reduction, is also debated. While photon energy is crucial, there is evidence that with ultrashort laser pulses, non-linear processes can occur, inducing photochemical reduction even at lower photon energies^{22,23}. At the same time, in some cases, the mechanism for photoreduction could be ascribed only to thermal effects for a wide range of wavelengths, surpassing the commonly agreed threshold for photochemical processes²⁴.

Previous studies have provided a reasonable understanding of the reduction mechanism for UV and IR ranges²⁵, but not differentiated between the photothermal and photochemical effects of visible and near-infrared (NIR) range laser irradiation on GO¹⁴, a persistent gap, with many contradictions, that this study aims to resolve. Here, we adopt a systematic approach to and clarify our understanding of GO reduction. We use continuous-wave lasers across the visible (405, 532, 633 nm) and NIR (785 nm) spectrum to simplify the system as much as possible and rule out the complexities and additional variables associated with pulsed lasers, such as heating/cooling cycles and influence of the pulse width, and two-photon absorption phenomena that arise with ultrashort pulse durations²⁶. This choice is guided by the hypothesis that the visible laser energy falls below the threshold commonly associated with photochemical reduction^{4,27}.

In this work, we used a robust comparative analysis between GO's thermal and laser-induced chemical changes to elucidate the reduction mechanism. Determining the temperatures reached under laser irradiation is the most challenging part of such a study. Here, we employ Raman thermometry for real-time temperature measurement during laser reduction, allowing us to distinguish between photothermal and photochemical contributions in situ. The most direct estimation of the degree of reduction was obtained using X-ray photoelectron spectroscopy (XPS). This comprehensive method is the tool of choice to assess the surface chemical composition and structure

and thus to investigate chemical reactions. In addition, other commonly used methods to assess GO reduction, such as Raman bands intensity ratio or peak shift, were omitted due to the high defect density of rGO that produces broad D and G bands with little correlation to the degree of reduction^{28,29}. Moreover, rGO structures in this work were done in a single laser spot, having spatial dimensions of several micrometers, leaving other common characterization methods, such as FTIR, out of the scope. Thus, to assess the electronic properties and work function changes in reduced GO, thereby evaluating the degree of reduction and its impact on material properties at the single laser-spot level, we used current-sensing atomic force microscopy (CS-AFM) and Kelvin probe force microscopy (KPFM)³⁰.

Our findings provide a more coherent and detailed understanding of the laser-reduction mechanisms of GO. By combining advanced spectroscopic techniques and nanoscale analyses, we offer clarity in a field marked by contradictory findings, contributing to fundamental research and potential technological applications. Building on these insights, we showcase this potential by pioneering light-encoding secure information within GO films. These patterns remain invisible to the naked eye and undetectable by conventional optical microscopy.

Results

In our experiments, we used indium tin oxide (ITO)-coated glass substrates covered with a GO film. Unless stated otherwise, the film thickness was 10 nm. GO was subjected to laser-induced reduction by varying the laser wavelength from visible to NIR and finely adjusting the laser power for each irradiated spot, which ranged from a few micro-watts (μW) to several milli-watts (mW). The reduction time was 1 min. for all treatments unless specified otherwise. To prevent additional reduction of the GO film during Raman and photoluminescence (PL) spectroscopy measurements, we set the laser power to the lowest feasible level. Although the laser power varied with each specific laser used, it remained in the μW to a few-mW range.

PL and Raman spectra at different laser powers

Figure 1 shows the schematic representation of our experiments: the GO film subjected to laser treatment and combined with silicon nanowires (SiNWs) on an ITO/glass substrate and its optical response (Fig. 1b–d). SiNWs play a critical role as an in situ thermometer, thus allowing us to quantify temperature variations under different laser powers and wavelengths. Unfortunately, when recorded using the 785 nm laser, the Raman spectra did not exhibit any Si signals due to interference in the CCD detector. Consequently, our temperature-dependent studies focused on three wavelengths: 405, 532, and 633 nm. Despite this, findings derived from these three lasers can be extrapolated to the NIR laser due to its similar behavior.

Untreated GO films are characterized by a prominent photoluminescence band centered around 690–730 nm (1.8–1.7 eV) (Fig. 1b). This band can be excited using blue (405 nm), green (532 nm), and red (633 nm) lasers, as depicted in Fig. 1b. An interesting observation was that increasing the laser power resulted in a decrease in the PL intensity. To illustrate this, when the laser power for the 532 nm laser was progressively increased, there was a substantial reduction in the PL band's intensity without any significant spectral shift. This behavior is shown in Fig. 1c, where the integrated PL intensity across the full spectrum (hereafter referred to as PL intensity) is plotted against the laser power. A drastic PL intensity drop was observed upon increasing the laser power, which plateaued starting from around 300 μW and is well described by the exponential decay function in Fig. 1c. This decay in PL emission was universally observed across all employed laser wavelengths and manifested at similar laser power levels, as can be seen in Supplementary Fig. 1a, c, e. In a related study²⁹, we noted that the GO film's conductance increased as the laser irradiation power (532 nm, continuous-wave (CW) laser) rose following a similar exponential behavior, plateauing at ≈ 1 mW. These results suggest a

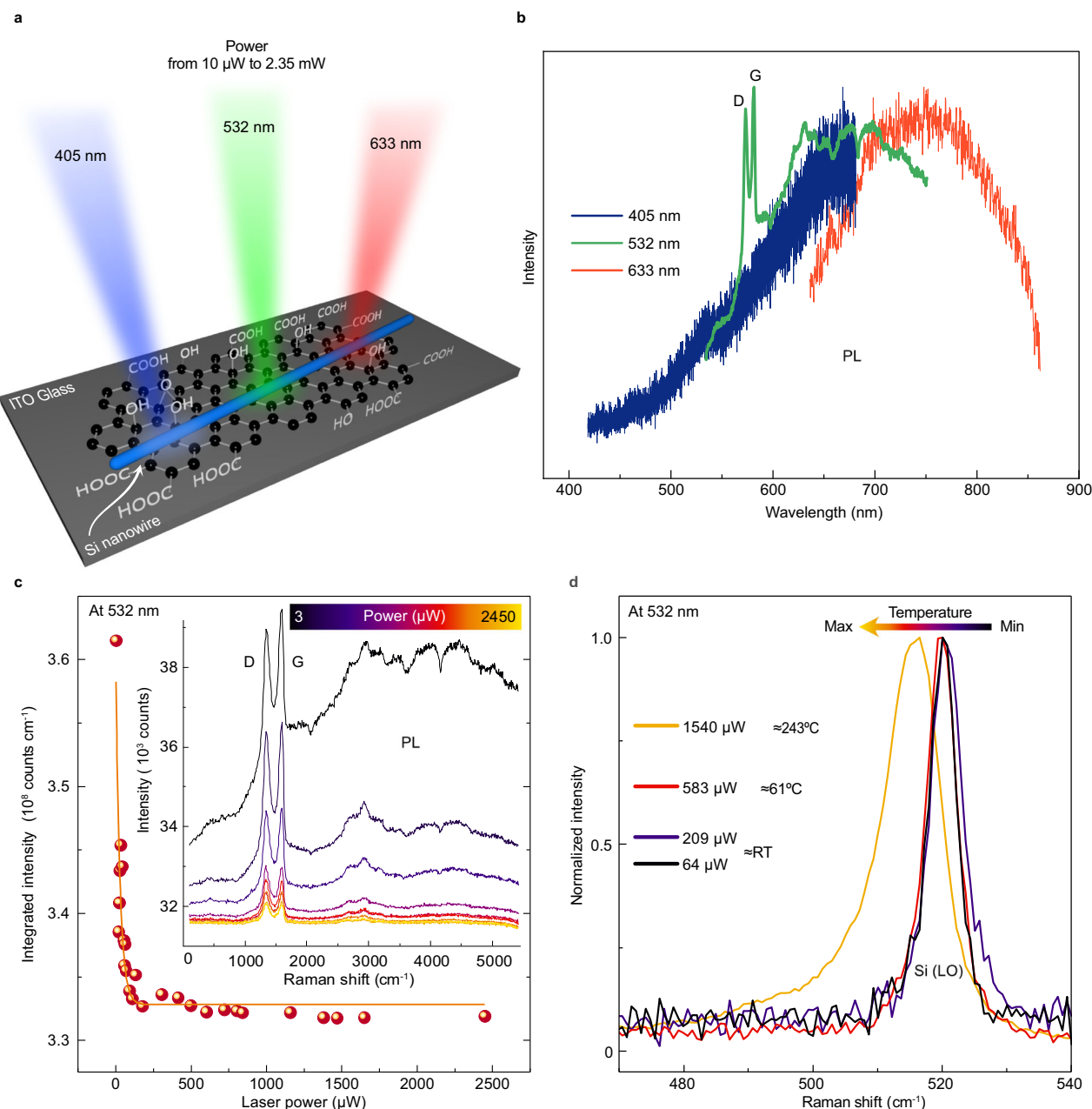


Fig. 1 | Raman thermometry and PL quenching during laser reduction of GO. **a** Sketch of the laser-reduction experiment of GO film mixed with SiNWs on ITO/glass substrate with different wavelengths and laser powers. **b** Raman spectra of GO film under different laser excitation wavelengths at constant powers below 10 μW with D and G Raman peaks marked. **c** Non-linear decay of PL peak area (Integrated intensity) versus applied laser power for 532 nm laser. The solid line is a fit given by

an exponential decay function $y = y_0 - A_1 e^{-x/\tau_1}$. The inset with raw data demonstrates the power-dependent Raman spectra used for the integrated intensity calculation. **d** Si NW Raman peak shift is driven by the photothermal effect (532 nm laser) in GO/SiNWs film. The temperatures achieved at each laser power are specified. Source data are provided as a Source Data file.

discernible laser power, indicative of a complete laser-driven modification of the GO film.

Simultaneously, the intensity ratio of the D to G Raman bands, a standard metric for assessing GO reduction, remained unchanged as the laser power on GO films varied, as evidenced by results in Fig. 1c. Several reports, including one from our group²⁹, highlighted the limited insights provided by the D/G ratio for both GO and rGO^{5,21}. A constant D/G ratio for GO and rGO can be observed in scenarios with a high defect density or when subjected to low-temperature treatments forming highly defective structures of rGO⁵. These conditions lack the energy required to drive the graphene lattice reconstruction.

Evidencing thermal effects through Raman thermometry

We focused on measuring the in situ temperature changes induced by laser irradiation to investigate the role of photothermal effects in our samples. We introduced SiNWs atop the GO film for this purpose and realized the concept of Raman thermometry. This method is based on the shift in the Raman peak of SiNWs when subjected to heat. With increased laser power, there was a noticeable downward shift in the Si LO peak at 520.7 cm^{-1} due to the photothermal expansion of silicon's diamond-like crystal structure, as depicted in Fig. 1d. A thorough explanation of this method is provided in the Materials and methods section. We determined the temperature values using the Raman peak-shift temperature coefficient³¹ of $-0.022 \text{ cm}^{-1} \text{ } ^\circ\text{C}^{-1}$.

The most marked changes in PL were observed at temperatures significantly below 120 °C for all the wavelengths investigated, as shown in Supplementary Fig. 1.

PL arising from low-energy transitions is typically associated with electronic transitions involving adsorbed water, which is known to facilitate the least energetic radiative transition in GO³². Based on these findings, we deduce that the observed PL reduction at these temperatures can be attributed to the combined effects from the desorption of water molecules and -OH groups elimination or temperature-induced effects.

To validate the threshold temperature necessary for the PL quenching in GO, control experiments were conducted using temperature-dependent Raman spectroscopy on GO films, as depicted in Supplementary Fig. 2. In this case, the GO films were subjected to incremental heating on a heating plate, during which both Raman and PL spectra were simultaneously recorded at minimal laser power. It was observed that the PL emission from the GO films diminished progressively with an increase in temperature, plateauing at around 140 °C. The quenching of PL emission proved to be a reversible phenomenon, as evidenced by the recovery of PL upon cooling, provided the thermal treatment did not exceed 120 °C (see Supplementary Fig. 3). However, this reversibility starkly contrasts with the behavior observed under laser irradiation, where the reduction in PL intensity was irreversible even at comparably lower temperatures. This mismatch points to a fundamental distinction in the mechanism driven by laser irradiation compared to thermal annealing.

This scenario is significantly different when the thermal treatment exceeds 140 °C. At these higher temperatures, the PL background signal drops irreversibly, persisting at this low intensity even after cooling back to room temperature. The behavior between the 120 and 140 °C threshold can be attributed to the onset of reduction, characterized by the removal of oxygen-containing functional groups from GO. This, in turn, has several consequences: the material's electronic structure is altered, which is reflected in rGO electrical conductivity. Meanwhile, polar functional group removal increases the material's hydrophobicity, hindering the reabsorption of water molecules. Both explain the irreversible PL quenching we observed. Reversible PL quenching in the case of heating below the reduction threshold is attributed to thermal PL quenching and the reversibility of water desorption after cooling. Additionally, we do not exclude the reversible reduction of GO, where at relatively low temperatures, GO could be reduced and oxidized back once cooled down to room temperature, as was shown in the case of photothermal reduction³³. The reversible reduction might be considered an additional effect contributing to the reversible PL quenching at temperatures below the threshold.

We obtained complementary evidence for this thermal reduction threshold through thermogravimetric analysis (TGA), as depicted in Supplementary Fig. 4. The initial mass loss, correlating to the desorption of water, was observed at ≈ 100 °C. The onset of GO reduction, marked by a secondary mass loss, started around 140 °C. These observations suggest that the irreversible reduction process of GO is initiated at this temperature, corroborating the thermal profile deduced from the PL data and further elucidating the distinct pathways of thermal and laser-induced GO modifications.

Considering the reversible nature of the PL drop following thermal treatment, we suspected that thermal quenching of PL does not play a role in the laser processing experiments, given that the spectral data were acquired immediately after irradiation. To confirm that the decrease in PL did not result from thermal effects, we conducted an experiment using a 532 nm laser at a low power of ≈ 86 μ W, which caused only a minor temperature increase of around 50 °C. However, Raman spectra collected from the same location after irradiation with low-power lasers showed that the decrease in PL was irreversible (as seen in Supplementary Fig. 5a). Irreversibility in PL decrease was also

observed using red and NIR lasers, indicating a photochemical mechanism rather than a photothermal effect (see Supplementary Fig. 5b, c).

Further, we investigated how the GO film thickness affects the reduction process, an essential factor for optical transmission and, subsequently, the temperature reached during laser irradiation. We prepared GO films with thicknesses around 50, 110, and 500 nm as determined by AFM results in Supplementary Fig. 6a–c. Each film was irradiated with a 532 nm laser and different powers to compare PL decays. We found that PL decay does not depend on the film thickness, meaning that PL emission vanished at the same laser power used (Supplementary Fig. 7d). The only difference observed between these films was the initial PL intensity, which was expected since more material emits more photons. Assuming that thicker films have higher temperatures under laser irradiation, the independence of PL on the film thickness is further evidence of the photochemical nature of the reduction process. Additionally, we examined the reduction of the thin film consisting of one to three GO layers (Supplementary Fig. 7a) following the same protocol of measuring PL intensity versus laser power. We observed that for a thin film, the reduction process goes slightly faster with the PL disappearance at the laser power of several μ W (Supplementary Fig. 7b). This change in the reduction rate might be attributed to the less-pronounced interlayer interaction and intercalation, which facilitates the reduction process. Moreover, the GO monolayer has low transparency and experiences insignificant heating; thus, its laser-induced reduction, even at low laser power, further supports the photochemical reduction mechanism.

Given that the photon energies associated with blue (3.06 eV), green (2.33 eV), red (1.96 eV), and NIR (1.58 eV) lasers are below the threshold required for the photochemical dissociation of epoxy groups (3.2 eV), the likely scenario involves the cleavage of hydroxyl group bonds, which possess the smallest bond energy of 1.5 eV from all the oxygen functionalities¹⁹. Furthermore, the energy of the lasers used in this investigation is insufficient to break other oxygen bonds¹⁹. Nevertheless, the secondary transformations induced by laser irradiation could lead to the cleavage of -COOH or C–C bonds conjugated with C=O groups. This would result in decreased C=O component intensity in the XPS spectra, which will be discussed later. This bond cleavage changes the chemical composition of the GO, its electronic structure, and its interaction with water, resulting in the irreversible change in PL.

Discrepancies between simulations and Raman thermometry

We developed a photothermal model that analyzes heat dissipation and temperature gradients to elucidate the thermal dynamics induced by laser irradiation in the GO/ITO/glass system. We focused exclusively on thermal effects by simplifying the model and neglecting factors such as chemical and optical changes during irradiation and the presence of adsorbed water. This simplification could overestimate the temperatures compared to experimental observations, with any deviations highlighting potential non-photothermal pathways for energy dissipation.

Our simulation results in Fig. 2 predicted the most intense temperatures at the laser focal point to be 279, 371, and 975 °C for the red, green, and blue lasers, respectively. The laser-induced heated zones were calculated to be less than 1.4 μ m in diameter, generating roughly 7 μ m across highly localized hotspots. Fitting the simulation results model, which considered only thermal conduction, shows a linear correlation between the laser power and the temperature of GO; however, the experimental temperature results from Raman thermometry show scattered values. Linear fits of these data produced slope values indicating the efficiency of photothermal conversion, which differed significantly from the linear fits to simulated results. The blue laser (405 nm) demonstrated a relatively modest slope of 0.04 ± 0.01 °C μ W⁻¹, suggesting weaker photothermal transduction

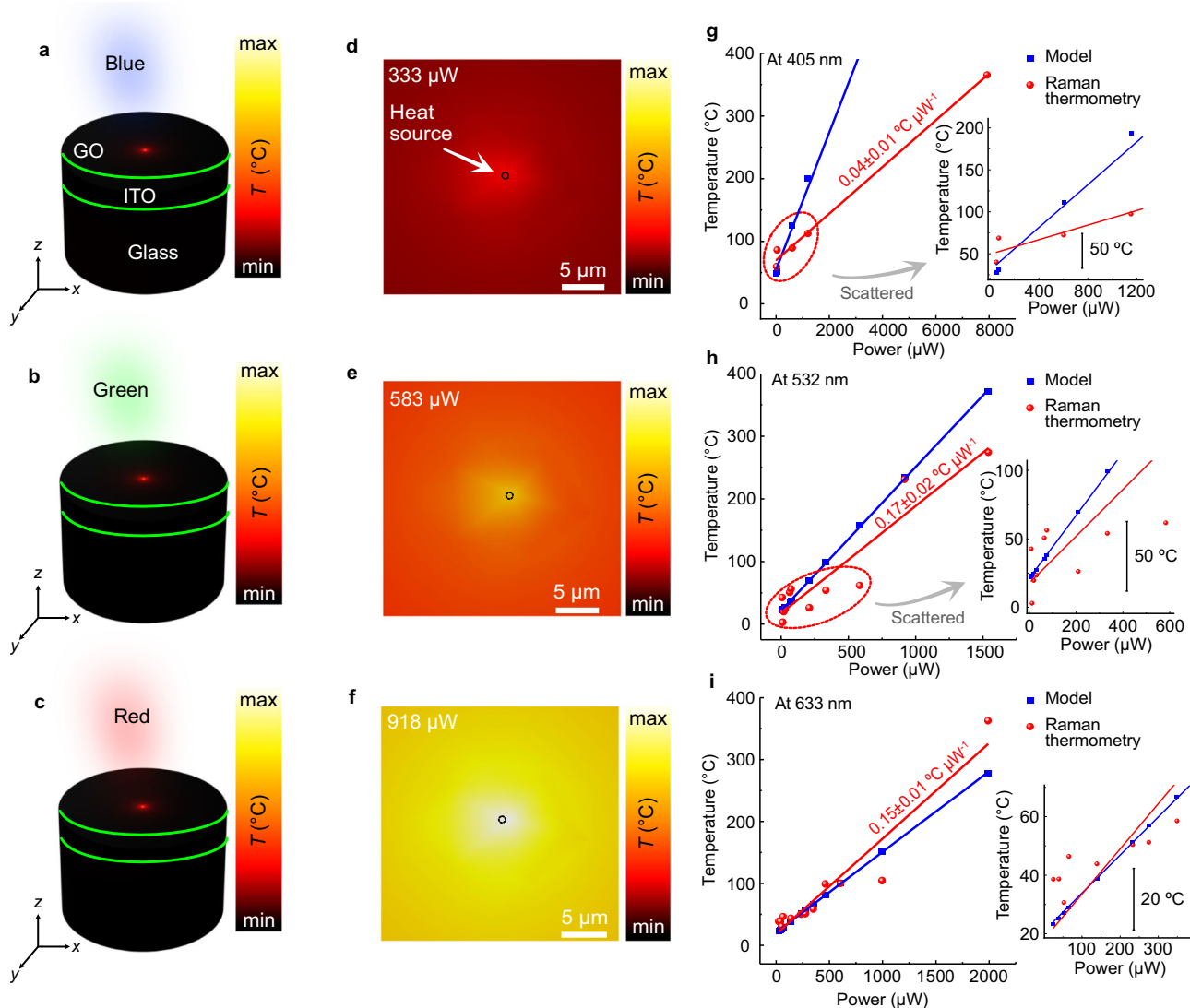


Fig. 2 | Comparison of the temperatures extracted from the model with Raman thermometry. **a–c** Panels depict finite element method (FEM) simulated thermal distributions at the surface of a GO/ITO/Glass sample when exposed to 405 nm (blue), 532 nm (green), and 633 nm (red) laser irradiation. **d–f** Panels showing temperature profiles at specific power outputs. The heat source and the temperature scales highlight the precision of localized heating. **g–i** Panels show the

corresponding temperature versus power plots, comparing FEM model predictions (blue squares) with experimental data obtained through Raman thermometry (red circles). The slopes of the fitted lines illustrate the relative efficiency of photo-thermal conversion for each laser wavelength. Zoom-ins around the low laser power regions with scattered data points are presented as insets. The color scales are linear. Source data are provided as a Source Data file.

compared to the green (532 nm) and red (633 nm) lasers, which displayed larger slopes of $0.17 \pm 0.02 \text{ } ^\circ\text{C } \mu\text{W}^{-1}$ and $0.23 \pm 0.01 \text{ } ^\circ\text{C } \mu\text{W}^{-1}$, respectively.

This divergence in slope values evidences a critical consideration in the photothermal versus photochemical behavior as a function of laser wavelength. The lower efficiency in photothermal heating by the blue laser, as evidenced by its lower slope, hints that its photon energy may preferentially drive photochemical reactions rather than contribute to heating. This is further corroborated by the observation that the temperature under the blue laser at 1 mW barely exceeds $100 \text{ } ^\circ\text{C}$, which is considerably less than the $230 \text{ } ^\circ\text{C}$ recorded under the green laser, even though the blue laser matches the GO's optical absorption peak better with a 10% higher absorption than that for the green and red lasers as shown in Supplementary Fig. 8.

The discrepancies observed lead us to propose that the blue laser's energy is not completely transformed into thermal energy; instead, a substantial portion of it likely facilitates the breaking of

chemical bonds, inducing photochemical reactions. This is a valuable insight, as it suggests that the absorbed energy at 405 nm contributes less to photothermal heating and more to direct photochemical reduction of GO. Such a mechanism is consistent with the reduction effects we observed at lower temperatures, which would be insufficient if a purely thermal mechanism were at play, thus stressing the crucial role of photochemistry in the reduction process.

The scattered nature of the experimental points in the temperature versus power plots shown in the insets in Fig. 2, as opposed to the clear linear trend predicted by simulations, indicate complexities in the physical processes that a purely photothermal model can not capture.

Thermal effects on the kinetics of PL decay

We investigated the kinetics of photoluminescence decay under various experimental conditions to further elucidate the underlying

mechanisms of GO reduction and corroborate the role of photochemical processes. By observing the changes in PL intensity over time, we figured out the dynamics of the reduction reaction occurring within the GO films. The kinetics of the OH groups cleavage follow a first-order behavior represented by Eq. (1):

$$\ln \frac{I_t}{I_0} = -k_d \cdot t \quad (1)$$

where I_t is the PL intensity at time t , I_0 is the initial PL intensity, and k_d is the first-order rate constant.

Our observations indicated that the rate constants remained invariant over a laser power range of 8 to 62 μW for a 532 nm laser, as detailed in Supplementary Fig. 9a. Additionally, no variation in the rate constants was seen across different photon energies, from 1.58 to 2.33 eV, as shown in Supplementary Fig. 9c. This invariability suggests that the photon energy is above the threshold for photolytic activation across all lasers utilized, supporting a photochemically driven reaction mechanism.

We conducted PL decay kinetics studies at a fixed laser power to further test for thermal effects while varying the sample temperature from room to 80 $^{\circ}\text{C}$ (Supplementary Fig. 9b). The independence of the reaction rate from temperature in this range reinforced the predominance of photochemical pathways. This finding was vital, as it confirmed that the observed reduction of GO is not significantly influenced by thermal contributions within the studied temperature range and is instead predominantly driven by photon-induced chemistry.

Nanoscale electronic profiling with atomic force microscopy

To validate the changes induced by low-power laser irradiation in GO at the nanoscale, we implemented CS-AFM and KPFM techniques to analyze GO/ITO/glass samples. CS-AFM was instrumental in determining the electrical resistance of discrete laser-modified spots on the GO film's surface, with results in Fig. 3.

The spot created by the blue laser exhibited the largest conductivity (Fig. 3d–f and Supplementary Fig. 10), which implies a more extensive reduction of GO at these locations. This enhancement in conductivity, especially prominent with the blue laser despite its associated temperature being significantly lower than those produced by the green and red lasers, is indicative of photon energy directly engaging in the cleavage of chemical bonds, thereby reducing GO and supporting our conclusions from Raman spectroscopy.

We observed an interesting trend: the conductivity around a laser-treated spot scaled with the wavelength of the laser, increasing from infrared to ultraviolet. CS-AFM was employed to examine spots created using different laser wavelengths but at the same optical powers to corroborate these results. We found that as the optical power increased, so did the conductivity of the laser-irradiated GO, irrespective of the laser wavelength. Figure 3c illustrates that the conductive region generated by the blue laser is markedly more extensive than those by the red (Fig. 3a) and green (Fig. 3b) lasers, which could be attributed to a larger spot size produced by the blue laser (due to the optical system). This relationship between laser wavelength, spot size, and induced conductivity shows the nuanced interplay between laser parameters and the resultant electrical properties of GO at the nanoscale.

Complementing the CS-AFM analysis, KPFM results further substantiated the disparity in reduced areas as a function of laser wavelength. The laser's power not only influenced heat dissipation but also unraveled complex phenomena, such as the presence of Airy ring patterns and the modulation of contact potential difference (CPD). The latter, a quantifiable indicator of surface work function variations, is crucial in assessing the extent of GO reduction.

Equation (2) can be used to evaluate the work function differences attributed to the reduction level in a thin GO layer³⁴:

$$V_{\text{CPD}} = \frac{\phi_{\text{tip}} - \phi_{\text{sample}}}{e} \quad (2)$$

where V_{CPD} is the contact potential difference measured between the AFM tip and the sample surface, e is the electron charge, and ϕ_{tip} and ϕ_{sample} are the tip and sample surface work functions, respectively. According to this relationship, an increase in work function leads to a decrease in CPD. Huang et al.³⁴ recently elucidated this correlation with the precise manipulation of the work function via the degree of GO reduction under green laser irradiation. Their findings revealed an increment in the work function corresponding to the intensity of the laser power, with the capability to fine-tune the work function at the meV level.

The decrease in work function is commonly used as an indicator of laser-induced GO reduction^{4,5}. However, the interplay between the green laser's power and the effects on GO requires closer examination. At a laser power of $\approx 600 \mu\text{W}$, the coherent photon flux was sufficient to generate pronounced interference patterns that appear as Airy rings—signatures of single-mode Raman laser beams—as presented in Fig. 3a. The CPD diminished at the irradiated center while increasing at the periphery and along the Airy rings (with the first ring exhibiting a CPD of $V_{1\text{st ring}} = (14.08 \pm 0.01) \text{ mV}$ and the second ring showing $V_{2\text{nd ring}} = (6.86 \pm 1.09) \text{ mV}$). As the optical power intensified, the lower-order Airy rings vanished. This is attributed to heat dissipation around the spot, further supporting a photochemical reduction pathway in GO at low laser powers. Moreover, precise laser beam signatures like Airy rings are less likely to arise from photothermal processes due to their relatively low intensity compared to the beam's center. Besides, GO reduction resulted in CPD changes but did not cause any detectable morphological changes even at relatively high laser powers (Supplementary Fig. 11).

In the case of red laser irradiation, shown in Fig. 4b, the rGO CPD was larger than that of the pristine GO but did not significantly increase with higher optical power. This observation aligns with temperature-dependent experiments on GO, where the high-intensity PL peak did not recover after heating to comparable temperatures, suggesting the lack of water readsorption. The CPD increase is a known response of GO at different humidity levels³⁵.

Conversely, the 405 nm laser treatment, illustrated in Fig. 3c, led to an unexpected CPD reduction, indicating an increase in the work function of rGO relative to GO. Moreover, the observed increase in spot diameter for the 405 nm laser, depicted in Fig. 3d, is noteworthy, especially considering that the spot sizes were similar across all wavelengths at lower powers. This phenomenon may be attributed to effects such as back reflection from the ITO/glass interface, causing the beam's footprint to be larger for 405 nm compared to other wavelengths.

These observations show that the electronic structure of GO was modified from a semiconductor and metal-like (depending on the degree of reduction), which can explain the irreversible PL quenching. On the other hand, the reversible PL quenching in the case of thermal annealing below the reduction threshold is attributed to thermal PL quenching and reversible thermal-induced water desorption.

Deciphering GO reduction through XPS

XPS was used to elucidate the chemical transformations that occurred in GO films due to laser irradiation. Micro-XPS mapping was employed to capture the chemical landscape's evolution by comparing the C1s and O1s region intensities from the survey spectra. We observed a clear trend when treating GO films with a 405 nm laser. As laser power increased, there was a progressive increase in the carbon-to-oxygen (C/O) ratio, indicative of GO's reduction (Fig. 5a). The survey spectra

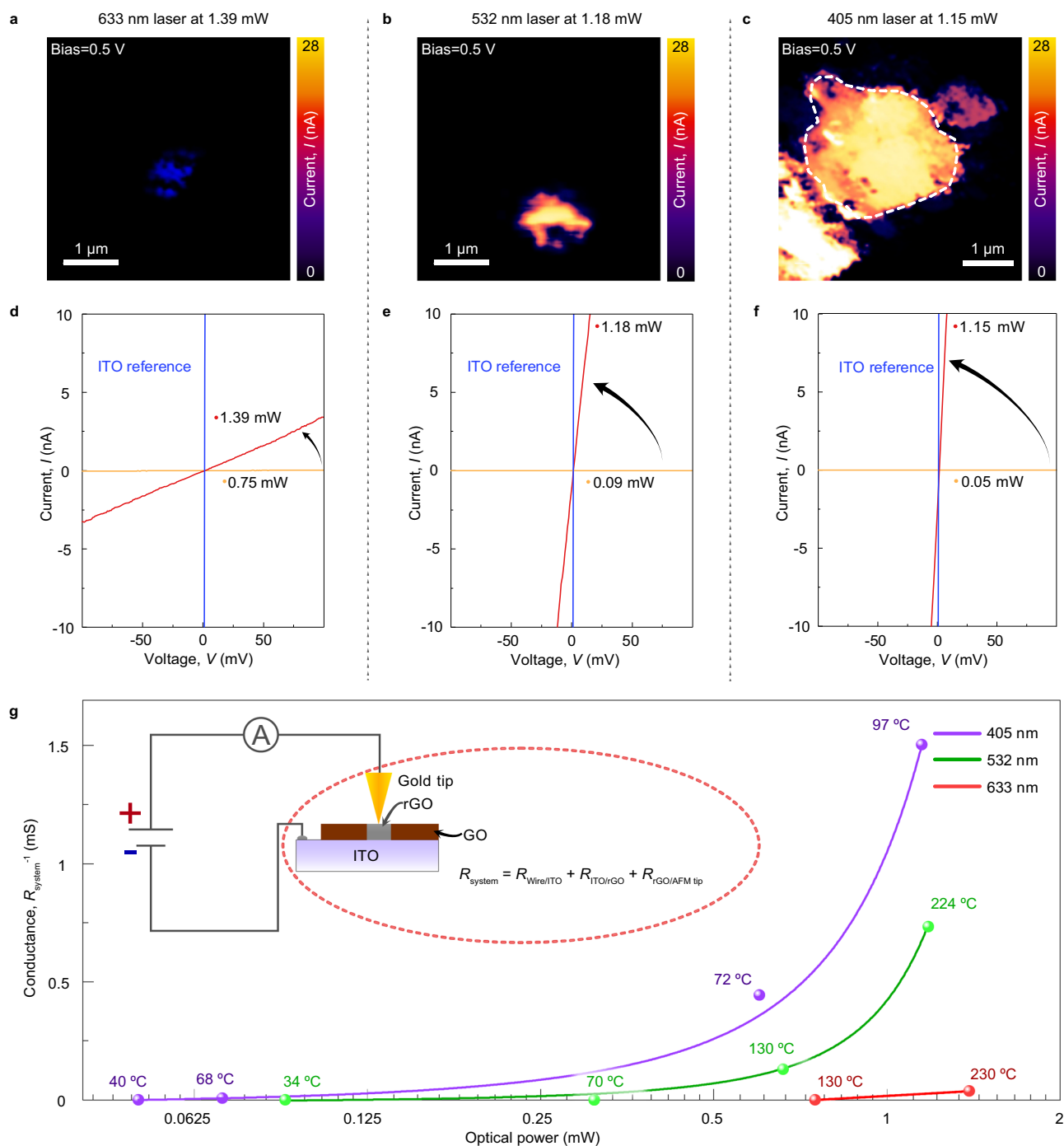


Fig. 3 | Electrical measurements of laser-reduced GO. **a–c** Current-sensing AFM imaging of laser-irradiated spots made under different wavelengths and similar optical powers. **d–f** Current-voltage characteristics from individual spots obtained at low (orange) and high (red) laser powers and wavelengths (see I/V characteristics for all utilized powers in Supplementary Fig. 8). ITO is taken as a reference (blue).

g Conductance as a function of optical power and temperature on the spots at different irradiation powers. The inset shows the electrical scheme and measured resistance represented by the sum of contact resistances between wire and ITO, ITO and rGO, and rGO and AFM tip. Temperature values for each laser power were obtained by Raman thermometry. Source data are provided as a Source Data file.

comparison for pristine GO and samples reduced by laser at powers of 1.2 and 7.4 mW is presented in Fig. 5b.

Three specific points were selected for an in-depth chemical compositional analysis: a pristine GO region serving as the baseline, a point subjected to the laser power (≈ 7.4 mW) where the C/O ratio peaked, and an intermediate point (≈ 1.2 mW). The corresponding temperature induced by laser irradiation with the laser power mentioned above was experimentally estimated to be ≈ 300 °C and ≈ 80 °C,

respectively. High-resolution C1s spectra revealed an increase of the C=C peak at 284.2 eV and a drop of C-C (284.8 eV), C-O (286 eV), C=O (287.3 eV), and O-C=O (288.5 eV) signals^{36,37}. High-resolution C1s XPS spectra facilitated a more accurate calculation of the C/O ratios at these locations. We defined the figure of merit for the degree of reduction ratio as C-C ($sp^2 + sp^3$) and C-O (C-O + C=O + O-C=O) peak area ratio calculated from the C1s high-resolution spectra. This ratio was calculated to be 1.08, 1.91, and 2.32 for GO, ≈ 1.1 mW, and ≈ 7.4 mW

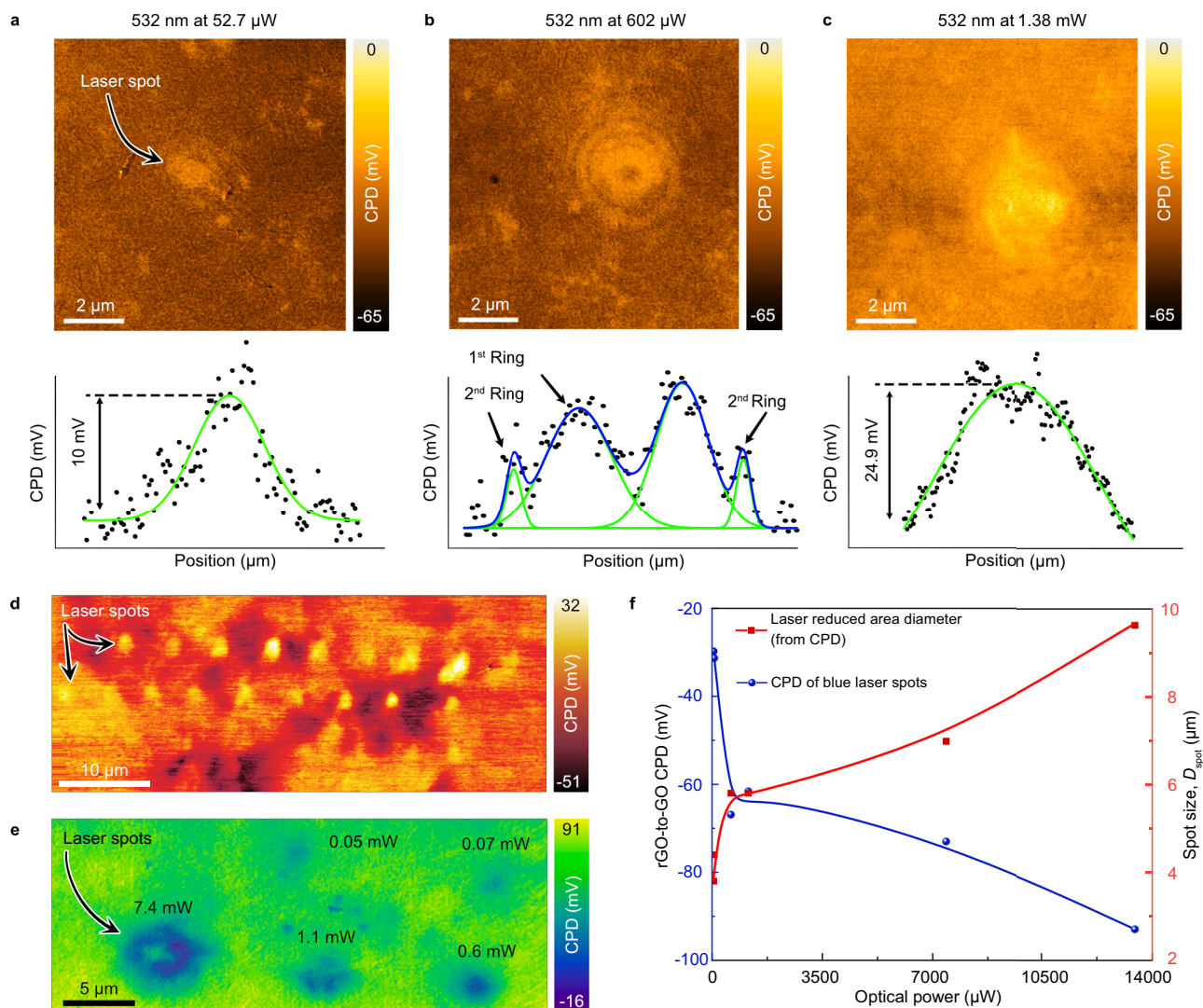


Fig. 4 | KPFM profiling of laser-induced spots. a–c CPD imaging by KPFM of single laser-irradiated spots on GO/ITO obtained at different laser powers with CPD profile (black spots—initial data, green line—fitting, blue line—common fitting line)

changes of rGO spots with respect to GO. **d** CPD of single laser-irradiated spots made by red laser and **e** blue laser. **f** CPD and diameter of a single spot versus 405 nm laser power. Source data are provided as a Source Data file.

samples, respectively (Fig. 5c–e). One could see a significant jump in this ratio from the pristine GO to reduced under ≈ 1.1 mW and then a slight increase at ≈ 7.4 mW, indicating that the most intense reduction occurred at the first step. In contrast, a further increase in laser power triggers the removal of residual oxygen functionalities. This process resulted in less pronounced chemical changes in the structure. Moreover, residual oxygen-containing group removal might also be triggered by the addition of thermal effects, which are expected to play a role at high laser powers.

The investigation was extended to the effects of 532 nm laser irradiation on GO. In this set of experiments, the Raman laser integrated within the XPS machine was utilized for precise spot irradiation and subsequent XPS analysis in situ. The high-resolution C1s spectra were deconvoluted into five distinct bands: sp^2 hybridized carbon at 284.2 eV, sp^3 hybridized carbon at 284.8 eV, C–O at 286 eV, C=O at 287.3 and O–C=O 288.5 eV^{36,37}. The initial C/O ratio in GO was ≈ 0.9 ; following laser exposure at 0.3 mW (power density ≈ 2.2 W cm⁻²), the ratio increased to 2.5, as shown in Supplementary Fig. 12. This indicated a chemical transformation, with the relative carbon content rising from 47.7 to 76.7% and a notable increase in the sp^2 component relative to sp^3 . Further, increase in the laser power did not significantly

change the C/O ratio, suggesting that reduction had been achieved even at this relatively low power level (Supplementary Fig. 13).

These XPS results collectively confirm our hypothesis: photon energy from laser irradiation is preferentially deployed in photochemical reactions, predominantly facilitating the cleavage of C–O bonds. This process effectively strips oxygen-containing groups from the GO structure, as evidenced by the increased C/O ratio and the restoration of the sp^2 carbon network. These photochemical transformations are consistent across the different laser wavelengths investigated here, establishing a coherent picture of the underlying mechanisms responsible for the photoluminescence decay observed in our study. The convergence of these findings with the photoluminescence and Raman thermometry data corroborates the prevalence of photochemical processes in the laser-induced reduction of GO.

To contrast thermal reduction and photoreduction, we performed an analysis of the chemical transformation induced by the thermal treatment by recording the XPS survey and C1s high-resolution spectra from a pristine GO sample and samples heated up to 80, 100, 120, and 140 °C. According to survey spectra, the elemental composition of thermally treated GO consisted of C (285 eV), O

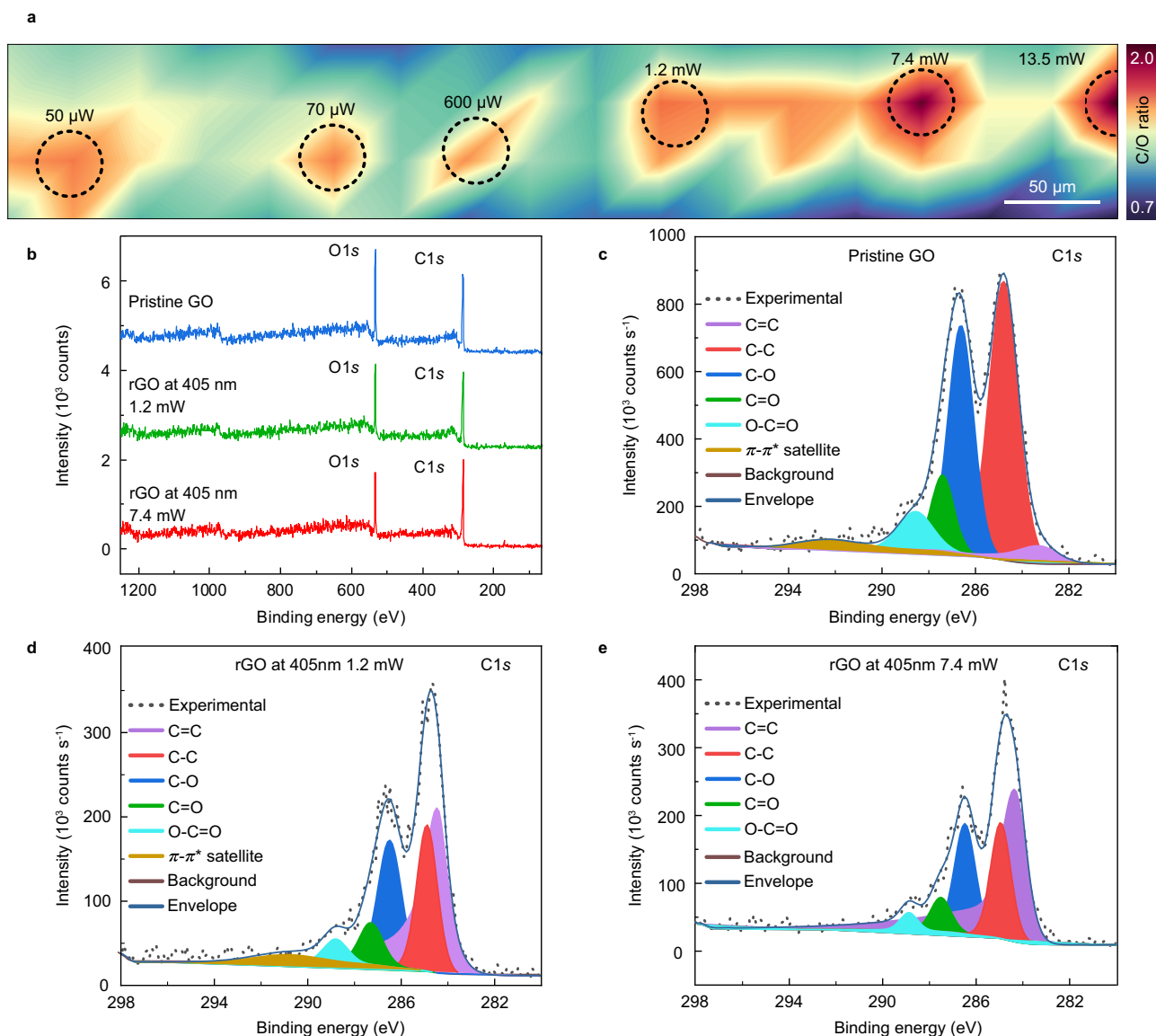


Fig. 5 | Study of rGO chemical composition by XPS. **a** Micro-XPS mapping illustrates the spatial distribution of the C/O ratio on a GO film following 405 nm laser irradiation. The dashed circles indicate the location of the laser-irradiated spots at laser powers of 50, 70, 600 μ W, 1.2 mW, 7.4 mW, and 13.5 mW from left to right. The color gradient from blue to red indicates an increase in the C/O ratio, a direct measure of GO reduction. **b** Survey XPS spectra differentiate between untreated GO (blue) and laser-reduced GO at 405 nm 1.2 mW (green) and 7.4 mW (red respectively). The rGO spectrum shows a C1s peak larger than the O1s peak,

indicating a decrease in oxygen content consistent with reduction. The data has been offset. **c–e** High-resolution C1s spectra reveal the detailed chemical structure changes from **c** GO to rGO with different laser powers of **d** 1.2 mW and **e** 7.4 mW. The GO spectrum shows peaks associated with various oxygen-carbon bonds. In contrast, the rGO spectrum displays a substantial rise in the C=C sp^2 bond peak, suggesting the restoration of the graphitic domain and a reduction in peaks associated with oxygen-containing functional groups due to laser irradiation. Source data are provided as a Source Data file.

(532 eV), N (408 eV), and S (172 eV). High-resolution spectra in the C1s region for thermally treated GO (room temperature, 80, 100, 120, 140 $^{\circ}$ C) were fitted with five distinct peaks corresponding to sp^2 hybridized carbon at 284–284.4 eV, C–C sp^3 hybridized carbon at 284.8 eV, C–O at 286.0–286.5 eV, C=O at 287.1–287.4 eV, and O–C=O at 288.0–288.5 eV (Supplementary Fig. 14). Significant spectral changes could be observed only for the sample treated at 140 $^{\circ}$ C, which explains the irreversibility of PL intensity reduction in these conditions. However, quantifying these changes is somewhat tricky since this temperature was found to be a threshold value where small structural changes could occur, making the quantification unreliable.

Summarizing the findings obtained from the XPS analysis of laser and thermally treated samples, we conclude that the alterations in the chemical structure of GO are much more pronounced for the laser-

treated samples even at low laser power, where temperatures were measured to be less than 100 $^{\circ}$ C. Such significant discrepancies in the induced structural changes directly support our conclusion on the dominant role of the photochemical reduction route.

Laser-induced PL quenching in GO for optical encoding

Our findings on the laser-induced irreversible quenching of GO's photoluminescence hold implications for optical data storage. It is determined that below a certain laser power threshold, areas of GO subjected to laser irradiation are visually identical to non-irradiated regions, enabling a form of optical encoding invisible to the naked eye. This phenomenon could serve for data storage: pristine GO, with its inherent PL, represents a binary "0", while modified areas with quenched PL, corresponding to reduced GO, represent a binary "1".

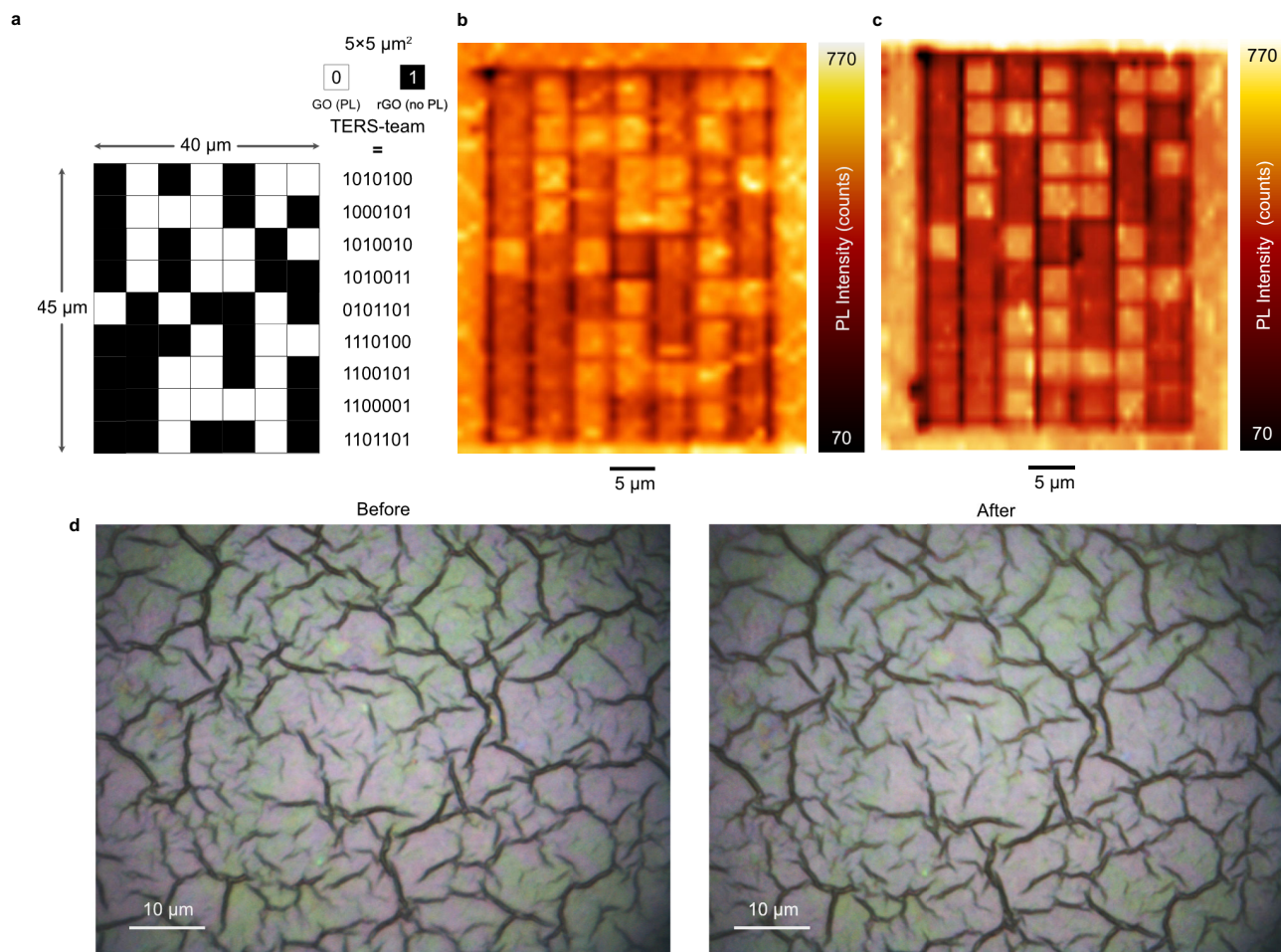


Fig. 6 | Laser-induced PL quenching in GO for optical encoding. **a** Schematic representation of the laser encoding process, where a focused laser beam selectively quenches photoluminescence in graphene oxide to record binary data. The binary code is based on the high PL signal from pristine GO indicating “0” and the low signal from reduced GO indicating “1”. The inset shows the binary encoding and a 7-bit ASCII representation of “TERS-team” encoded onto the GO film. **b, c** Raman

microscopy image displaying the encoded binary information on a GO film, where the dark squares represent reduced GO with quenched PL (“1”), and the bright squares correspond to unirradiated GO (“0”) on September 2023 (**b**) and March 2024 (**c**). **d** Optical micrographs of the GO film before and after the laser encoding process demonstrate the invisibility of the encoded data.

This optical encoding method was implemented, as illustrated in Fig. 6a, where the text “TERS-team” was encoded into a 7-bit ASCII binary sequence and patterned onto a GO film. This pattern was created using a 532 nm laser at a fine-tuned power of 62.9 μW . We used Raman spectroscopy at a non-reductive power setting of 12.8 μW to retrieve the stored information without further altering the sample. This allowed us to distinguish between treated and untreated regions. The binary data can be sequentially read from the pattern, top to bottom.

The security of this encoding method is rooted in the specialized ability to discern the encoded patterns, which requires specific knowledge of the PL characteristics of graphene oxide and the proper tools for detection. This is akin to the invisible ink visible only under UV light; however, our method is substantially more sophisticated, offering higher information density and enhanced security measures. Moreover, the stored pattern is time stable, as evidenced by the readout of the very same pattern right after writing it and seven months after the encoding. After seven months, the encoded features could be clearly distinguished and the information could be restored from the pattern.

Our encoding strategy lies in its subtlety; by carefully choosing the laser power, we can encode data onto the GO film that remains concealed under standard optical microscopy examination, as shown

in Fig. 6d. This stealthy approach is promising for the advancement of optical memory storage technologies. This expectation is also justified by the ease of integrating this method into current manufacturing workflows, particularly those involving lithography, paving the way for secure, high-density data storage applications. Our research highlights the transformative potential of leveraging the distinctive nanoscale characteristics of GO and rGO.

Discussion

Our investigation offers a comprehensive understanding of the mechanisms underlying the laser reduction of graphene oxide using visible light. We have demonstrated that the process is not mainly photothermal, as previously hypothesized, but critically involves photochemical pathways through the cleavage of hydroxyl bonds.

X-ray photoelectron spectroscopy, current-sensing atomic force microscopy, and Kelvin probe force microscopy all substantiate that the alterations in GO’s structure occur at temperatures lower than those predicted by purely photothermal theories. Although the D and G band intensity ratios in Raman spectroscopy remained constant, there was a pronounced decline in broadband photoluminescence at temperatures below 100 °C. This reduction in PL, which did not revert even when the power was decreased, indicates the elimination of polar groups from GO’s structure. Besides, while

thermal treatments up to 120 °C allow for reversibility in PL intensity, laser-induced PL quenching is permanent, confirming the photochemical nature of the process. Kinetic analyses further corroborate that the rate of GO reduction remains constant across varying laser powers and photon energies, demonstrating a predominantly photochemical route unaffected by thermal effects. Our combined analysis with XPS, CS-AFM, and KPFM strongly supports the photochemical cleavage of oxygen-containing groups as the dominant mechanism in GO reduction under visible light. Nevertheless, direct observation of the photochemical bond cleavage at the single-bond level would likely provide direct proof of the mechanism. Future studies employing advanced in situ characterization could provide more direct insights into the photochemical processes involved. For instance, tip-enhanced Raman spectroscopy (TERS) has shown the capability for nanoscale imaging of GO and other carbon allotropes³⁸. Temperature and humidity-dependent TERS could provide a window into the laser reduction of GO. However, achieving single-functional-group resolution under these conditions is still challenging due to the inherent complexity of TERS and the fact that achieving molecular resolution has been possible in ultra-high vacuum and low-temperature conditions³⁹. Although direct evidence of functional group removal during laser reduction of GO at the molecular level remains elusive despite significant research efforts, the results provided in this work supports the hypothesis that a photochemical mechanism is responsible for the observed phenomena.

Our findings also demonstrate a data storage and encoding application in which binary information is encoded onto GO films through laser-induced PL quenching. This approach offers a path toward high-density, long-lasting, and secure optical memory storage.

In summary, our research reveals that visible-light laser irradiation can effectively reduce GO through photochemical pathways via the cleavage of -OH groups. This advances the understanding of GO chemistry and opens up additional technological applications, warranting further research to optimize such processes for technological advancements in material science.

Methods

Graphene oxide sample preparation

For the GO film preparation, 2 mg mL⁻¹ of GO aqueous dispersion (GraphenOx, ≈99.5% purity) was used. ITO glass was used as a substrate. The dip-coating method was used to deposit a GO film at a 50 mm min⁻¹ rate, lifting the ITO glass from the dispersion. The sample was dried in ambient conditions. The chemical composition of prepared GO films was represented mainly by C and O atoms, with ≈1.5 at.% of S and ≈1.8 at.% of N impurities, coming as a left byproduct from the typically used modified Hummers method synthesis⁴⁰.

Laser irradiation, Raman spectroscopy, and thermometry on GO films

For the laser irradiation and Raman spectroscopy, the NTEGRA Spectra II AFM-Raman system with 532, 633, and 785 nm was used. For the experiments with a 405 nm laser, the Renishaw InVia Basis Raman spectrometer was used. Laser spot diameters (FWHM) for each wavelength were 631 ± 42 nm for the 633 nm (Supplementary Fig. 15), 520 ± 40 nm for 532 nm (Supplementary Fig. 16), and 1.2 μm for the 405 nm.

Temperature-dependent Raman measurements were done using a coupled NTEGRA Spectra II AFM-Raman system equipped with the thermal table. Raman spectra were measured using a 100× objective, 532 nm diode excitation laser. Exposure time was 15 s. and accumulated eight times.

Raman thermometry was carried out by SiNWs acting as temperature probes. SiNWs were deposited on GO/ITO substrate by drop casting from an aqueous solution. The coefficient used to determine

the temperature from the Si peak shift was $-0.022 \text{ cm}^{-1} \text{ °C}^{-1}$, with a temperature of 25 °C (ambient conditions), and 520.7 cm⁻¹ peak position was taken as a starting point.

Raman thermometry requires validation as a rarely used approach. Our literature review revealed no known artifacts for this method; largely, the values are taken at their face value, even though it is hard to use any reference method to check it for this system^{31,41–43}. So, we performed several control experiments to verify its validity for our application.

- (1) To exclude the different phonon shifts for the Si peak for bulk Si and for Si NW, the Si peak shift was calibrated by measuring its position when heated by a heating table. The coefficient was found to be $-0.024 \text{ cm}^{-1} \text{ °C}^{-1}$, which agrees well with the literature data.
- (2) One could assume that the Si NW could absorb a significant portion of the laser radiation and heat up excessively, also affecting GO reduction around it. To verify that, the Si NW peak shift was measured as a function of the laser power on a glass substrate, and no peak position dependence vs. laser power was observed for the relevant powers.
- (3) On the contrary, it is plausible that the GO heat is not transferred to the Si NW, which would lead to underestimating the temperature. Due to the high FWHM of GO and rGO peaks and their possible modifications for reasons other than heating (i.e., due to reduction), following the GO peaks themselves to monitor temperature appears challenging. Therefore, the measurement duration was chosen to be 30 s. to ensure the establishment of thermal equilibrium. Additionally, a comparison of the temperature of the NW to the substrate temperature was obtained for MoS₂ flake with Si NW, and they were observed to have the same temperature⁴⁴.

AFM topography and KPFM experiments

Atomic force microscopy with related Kelvin probe force microscopy was carried out by the NTEGRA II AFM system. The image was recorded with a Pt-coated tip. For CS-AFM, a fully gold AFM tip was used.

FEM simulations

Heating by continuous laser irradiation was simulated as a fixed heat source in the center of the sample surface. The sample consists of several layers from top to bottom: GO/ITO/glass with the following thicknesses: 10 nm, 120 nm, and 0.7 mm, respectively. The size (diameter) of the sample was set to 1 mm. Parametric sweeps were performed in the specified power ranges for each laser. Several laser spot diameters were used in the laser heating simulations: 1.45 μm for the 633 nm laser, 0.7 μm for the 532 nm laser, and 1.2 μm for the 405 nm laser. The total Irradiation time for the GO/ITO/glass sample was set at 60 s. for all the lasers. All parameters used were chosen according to the experimental measurements to represent the closest possible conditions for the experiments. However, the model does not consider wavelength-dependent effects; therefore, the obtained quantities must be taken cautiously, while we consider the qualitative description of the thermal effects reliable.

Thermogravimetric analysis

TGA-DSC was carried out in an open alumina crucible under dynamic airflow, with a 100 mL min⁻¹ flow rate from ambient temperature to 700 °C and a heating rate of 5 °C min⁻¹.

UV-vis

UV-vis measurements were performed using an Analytik Jena SPECORD250+ spectrometer in the reflectance mode. ITO-coated glass was recorded as a background. Data was smoothed by adjacent-averaging (50 points) using OriginPro software (version: OriginPro 2021b (64-bit) SR2 9.8.5.212).

Optical encoding

The pattern was coded using a 7-bit ASCII system. It was established that a square with luminescence represents “0” while a square with noticeably lower luminescence represents “1”. Optical encoding was performed by 100× NA 0.7 objective, 532 nm diode excitation Raman laser at 62.9 μW power and 3.6 μm s⁻¹ scan rate, using an integrated lithography module in NTEGRA Spectra AFM-Raman system. The result was recorded with the same setup using 12.8 μW laser power.

X-ray photoelectron spectroscopy

Combined XPS and Raman spectroscopy measurements were performed using a Thermo Fisher Scientific XPS NEXSA spectrometer with a monochromated Al K_α X-ray source working at 1486.6 eV and Thermo Scientific iXR Raman Spectrometer with a 532 nm laser respectively. The survey study was analyzed using pass energy 200 eV and energy resolution 1 eV. For the high-resolution spectra, the pass energy was 50 eV, and the energy resolution was 0.1 eV. The analyzed area had 10 μm². The flood gun was used to charge compensation. Binding energy by setting the C–C signal from C1s correction was not applied.

XPS mapping was performed on an area of 0.13 mm² with a step size of 25 μm (232 points). Survey and high-resolution spectra were taken for each point at the C1s and O1s regions. A C/O ratio map was constructed by mapping the C1s and O1s signals (at 285 and 533 eV, respectively) intensities ratio from the survey spectra.

Raman spectra were obtained at 0.1 mW power with an acquisition time of 120 s per scan.

Data availability

The data that support the findings of this study are available from the corresponding authors upon request. Source data are provided with this paper.

References

1. Wan, Z. et al. Laser-reduced graphene: synthesis, properties, and applications. *Adv. Mater. Technol.* **3**, 1700315 (2018).
2. Rodriguez, R. D. et al. Laser-engineered multifunctional graphene-glass electronics. *Adv. Mater.* **34**, e2206877 (2022).
3. Brown, M. S. & Arnold, C. B. in *Laser Precision Microfabrication* (eds Piqué, A., Sugioka, K. & Meunier, M.) Ch. 4 (Springer, 2010).
4. Murastov, G. V., Lipovka, A. A., Fatkullin, M. I., Rodriguez, R. D. & Sheremet, E. S. Laser reduction of graphene oxide: tuning local material properties. *Phys. Usp.* <https://doi.org/10.3367/ufne.2022.12.039291> (2022).
5. Arul, R. et al. The mechanism of direct laser writing of graphene features into graphene oxide films involves photoreduction and thermally assisted structural rearrangement. *Carbon* **99**, 423–431 (2016).
6. Li, H. & Bubeck, C. Photoreduction processes of graphene oxide and related applications. *Macromol. Res.* **21**, 290–297 (2013).
7. Alam, S. N., Sharma, N. & Kumar, L. Synthesis of graphene oxide (GO) by modified hummers method and its thermal reduction to obtain reduced graphene oxide (rGO). *Graphene* **06**, 1–18 (2017).
8. Le, L. T., Ervin, M. H., Qiu, H., Fuchs, B. E. & Lee, W. Y. Graphene supercapacitor electrodes fabricated by inkjet printing and thermal reduction of graphene oxide. *Electrochem. Commun.* **13**, 355–358 (2011).
9. Lipovka, A. et al. Photoinduced flexible graphene/polymer nanocomposites: design, formation mechanism, and properties engineering. *Carbon* **194**, 154–161 (2022).
10. Smirnov, V. A. et al. Photoreduction of graphite oxide. *High. Energy Chem.* **45**, 57–61 (2011).
11. Wu, J., Lin, H., Moss, D. J., Loh, K. P. & Jia, B. Graphene oxide for photonics, electronics and optoelectronics. *Nat. Rev. Chem.* **7**, 162–183 (2023).
12. Hou, W.-C. et al. Photochemical transformation of graphene oxide in sunlight. *Environ. Sci. Technol.* **49**, 3435–3443 (2015).
13. Matsumoto, Y. et al. Photoreaction of graphene oxide nanosheets in water. *J. Phys. Chem. C. Nanomater. Interfaces* **115**, 19280–19286 (2011).
14. Sharif, A., Farid, N., Collins, A., Jilani, A. & O’Connor, G. M. Extensive reduction of graphene oxide on thin polymer substrates by ultrafast laser for robust flexible sensor applications. *Appl. Surf. Sci.* **613**, 156067 (2023).
15. Bhattacharjya, D. et al. Fast and controllable reduction of graphene oxide by low-cost CO₂ laser for supercapacitor application. *Appl. Surf. Sci.* **462**, 353–361 (2018).
16. Yeh, C.-N., Raidongia, K., Shao, J., Yang, Q.-H. & Huang, J. On the origin of the stability of graphene oxide membranes in water. *Nat. Chem.* **7**, 166–170 (2014).
17. Otsuka, H. et al. Transient chemical and structural changes in graphene oxide during ripening. *Nat. Commun.* **15**, 1708 (2024).
18. Yin, K. et al. Thermodynamic and kinetic analysis of lowtemperature thermal reduction of graphene oxide. *Nanomicro Lett.* **3**, 51–55 (2011).
19. Acik, M. et al. Unusual infrared-absorption mechanism in thermally reduced graphene oxide. *Nat. Mater.* **9**, 840–845 (2010).
20. Shen, Y. et al. Revealing hidden endotherm of Hummers’ graphene oxide during low-temperature thermal reduction. *Carbon* **138**, 337–347 (2018).
21. Mikhailov, S. *Physics and Applications of Graphene: Experiments* (BoD – Books on Demand, 2011).
22. Kymakis, E., Petridis, C., Anthopoulos, T. D. & Stratakis, E. Laser-assisted reduction of graphene oxide for flexible, large-area optoelectronics. *IEEE J. Sel. Top. Quantum Electron.* **20**, 106–115 (2014).
23. Bobrinetskiy, I. I. et al. Laser direct 3D patterning and reduction of graphene oxide film on polymer substrate. *Mater. Lett.* **187**, 20–23 (2017).
24. Mitra, S., Kamaja, C. K. & Katiyar, M. Facile formation of porous, multilayer reduced graphene oxide electrodes using electrophoretic deposition and flash sintering. *Carbon* **202**, 186–195 (2023).
25. Zhao, L. et al. Laser reduced graphene oxide electrode for pathogenic detection. *ACS Appl. Mater. Interfaces* **15**, 9024–9033 (2023).
26. Zhao, X. et al. Ultrafast carrier dynamics and saturable absorption of solution-processable few-layered graphene oxide. *Appl. Phys. Lett.* **98**, 121905 (2011).
27. Gómez-Mancebo, M. B. et al. Comparison of thermal and laser-reduced graphene oxide production for energy storage applications. *Nanomaterials* **13**, 1391 (2023).
28. Rodriguez, R. D. et al. Ion-induced defects in graphite: a combined Kelvin probe and Raman microscopy investigation. *Phys. Status Solidi* **216**, 1900055 (2019).
29. Ma, B., Rodriguez, R. D., Ruban, A., Pavlov, S. & Sheremet, E. The correlation between electrical conductivity and second-order Raman modes of laser-reduced graphene oxide. *Phys. Chem. Chem. Phys.* **21**, 10125–10134 (2019).
30. Negishi, R., Takashima, K. & Kobayashi, Y. Investigation of surface potentials in reduced graphene oxide flake by Kelvin probe force microscopy. *Jpn. J. Appl. Phys.* **57**, 06HD02 (2018).
31. Doerk, G. S., Carraro, C. & Maboudian, R. Temperature dependence of Raman spectra for individual silicon nanowires. *Phys. Rev. B Condens. Matter Mater. Phys.* **80**, 073306 (2009).
32. Narayanam, P. K. & Sankaran, K. Optical behaviour of functional groups of graphene oxide. *Mater. Res. Express* **3**, 105604 (2016).
33. Wu, J. et al. 2D graphene oxide films expand functionality of photonic chips. *Adv. Mater.* **31**, e2403659 (2024).
34. Huang, Y. et al. Customizing the reduction of individual graphene oxide flakes for precise work function tuning with meV precision. *Nanoscale Adv.* **2**, 2738–2744 (2020).

35. Salomão, F. C., Lanzoni, E. M., Costa, C. A., Deneke, C. & Barros, E. B. Determination of high-frequency dielectric constant and surface potential of graphene oxide and influence of humidity by Kelvin probe force microscopy. *Langmuir* **31**, 11339–11343 (2015).
36. Chen, X., Wang, X. & Fang, D. A review on C1s XPS-spectra for some kinds of carbon materials. *Fuller. Nanotubes Carbon Nanostruct.* **28**, 1048–1058 (2020).
37. Peng, B., Xu, Y., Liu, K., Wang, X. & Mulder, F. M. High-performance and low-cost sodium-ion anode based on a facile black phosphorus–carbon nanocomposite. *ChemElectroChem* **4**, 2140–2144 (2017).
38. Sheremet, E. et al. Nanoscale imaging and identification of a four-component carbon sample. *Carbon* **96**, 588–593 (2016).
39. Zhang, R. et al. Chemical mapping of a single molecule by plasmon-enhanced Raman scattering. *Nature* **498**, 82–86 (2013).
40. Anegebe, B., Ifijien, I. H., Maliki, M., Uwidia, I. E. & Aigbodion, A. I. Graphene oxide synthesis and applications in emerging contaminant removal: a comprehensive review. *Environ. Sci. Eur.* **36** (2024).
41. Saltonstall, C. B., Serrano, J., Norris, P. M., Hopkins, P. E. & Beechem, T. E. Single element Raman thermometry. *Rev. Sci. Instrum.* **84**, 064903 (2013).
42. Amira, Z., Bouyahi, M. & Ezzedine, T. Measurement of temperature through Raman scattering. *Procedia Comput. Sci.* **73**, 350–357 (2015).
43. Han, L., Zeman, M. & Smets, A. H. M. Raman study of laser-induced heating effects in free-standing silicon nanocrystals. *Nanoscale* **7**, 8389–8397 (2015).
44. Tran, T.-H. et al. Laser-Induced photothermal activation of multi-layer MoS with spatially controlled catalytic activity. *J. Colloid Interface Sci.* **654**, 114–123 (2023).

Acknowledgements

The work was supported by the Russian Science Foundation grant № 22-12-20027, <https://rscf.ru/project/22-12-20027/>, and funding from the Tomsk region administration. “Electronic components based on laser integration for the biocompatible/biodegradable flexible electronic devices”. Work was conducted using the equipment of the Tomsk Regional Core Shared Research Facilities Centre of National Research Tomsk State University. We thank Elizaveta Dogadina for her help with the figures and illustrations. Prof. Cheng acknowledges the funding of the National Natural Science Foundation of China (No. 52161145402, 52173133) and the Sichuan Science and Technology Program (No. 2023YFH0008). The authors thank Prof. Dr. Mekhman Yusubov for the essential support with Raman, AFM, and XPS instrumentation. The authors are grateful to the center of TPU’s “Physical and chemical methods of analysis” for XPS measurements.

Author contributions

M.F. Conceptualization, methodology, formal analysis, data acquisition and analysis, writing—original draft, and writing—review & editing. D.C. Methodology, formal analysis, data acquisition and analysis, writing—

original draft, writing—review & editing. A.A. Methodology, FEM modeling, writing—review & editing. A.G. Methodology, formal analysis, data acquisition and analysis, writing—original draft, writing—review & editing. G.M. Conceptualization, formal analysis, writing—review & editing. J.L. Formal analysis, writing—review & editing. C.C. Conceptualization, formal analysis, writing—review & editing. P.P. Conceptualization, formal analysis, writing—review & editing, resources. R.D.R. Conceptualization, formal analysis, writing—review & editing, visualization, supervision. E.S. Conceptualization, methodology, formal analysis, writing—review & editing, supervision, resources and funding acquisition, and project administration.

Competing interests

The authors declare no competing interests.

Additional information

Supplementary information The online version contains supplementary material available at <https://doi.org/10.1038/s41467-024-53503-y>.

Correspondence and requests for materials should be addressed to Chong Cheng or Raul D. Rodriguez.

Peer review information *Nature Communications* thanks Pavan Narayanam and the other, anonymous, reviewers for their contribution to the peer review of this work. A peer review file is available.

Reprints and permissions information is available at <http://www.nature.com/reprints>

Publisher’s note Springer Nature remains neutral with regard to jurisdictional claims in published maps and institutional affiliations.

Open Access This article is licensed under a Creative Commons Attribution-NonCommercial-NoDerivatives 4.0 International License, which permits any non-commercial use, sharing, distribution and reproduction in any medium or format, as long as you give appropriate credit to the original author(s) and the source, provide a link to the Creative Commons licence, and indicate if you modified the licensed material. You do not have permission under this licence to share adapted material derived from this article or parts of it. The images or other third party material in this article are included in the article’s Creative Commons licence, unless indicated otherwise in a credit line to the material. If material is not included in the article’s Creative Commons licence and your intended use is not permitted by statutory regulation or exceeds the permitted use, you will need to obtain permission directly from the copyright holder. To view a copy of this licence, visit <http://creativecommons.org/licenses/by-nc-nd/4.0/>.

© The Author(s) 2024